Development of an evaluation method of floating ring bearings by CFD with mesh motion

Y Wang and Y B Xiao

Key Laboratory for Thermal Science and Power Engineering of Ministry of Education, Department of Energy and Power Engineering, Tsinghua University, Beijing, 100084, People's Republic of China

E-mail: yan-wang16@mails.thu.edu.com

Abstract. Floating ring bearings (FRBs) are widely used in the high speed turbocharger for their robustness. This paper introduces a CFD calculation method to predict the performance of the FRBs. Two phase model is included in the calculation method and transit calculation with mesh motion is conducted to predict the vibration characteristics. The simulation results are compared with the experiment to validate this method. Results show the two phase effect is important in predicting the FRBs at low oil-supplied pressure. This method shows great capacity of predicting the ring-to-shaft speed ratio and the vibration characteristics.

1. Background

Turbochargers are widely used in the heavy vehicles to improve engine performances, reduce fuel consumption and emissions. And FRBs are used in the turbochargers for its damping capacity and reduced friction loss. Turbochargers are designed to work under high rotation speed. However, rotor vibration increases when shaft speed reaches a critical value. The vibration causes lots of noise that annoys the passengers.

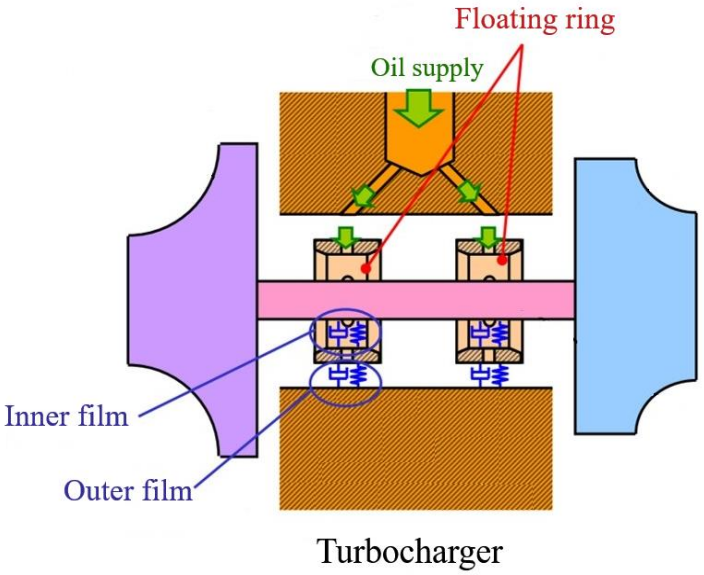

Figure 1. Turbocharger and floating ring bearing

Low oil-supplied pressure FRBs show the disappearance of the subsynchronous vibration at high shaft speed and are potential to reduce the noise. Hatakenaka et al [1] conduct experiment of FRBs at low oil-supplied pressure. Their results shows a sharp decrease of the ring-to-shaft speed ratio when shaft speed is larger than the critical value. Their results also indicate that the subsynchronous vibration disappears when shaft speed is larger than another critical value. The mechanism of these phenomenon are unclear. Many researchers have studied the FRBs and try to construct the prediction methods [2-4]. Trippett [5, 6] conducts the experiment of FRBs and reports the ring-to-shaft speed decrease. He assumed that the decrease in speed ratio is caused by the decrease in effective viscosity in the inner oil film due to the rise in temperature. Thermal effect then has long been assumed to be the cause of the decrease in speed ratio [7, 8]. San Andres and Kerth [7, 8] solve lumped energy equation with viscous heat generation and consider convective heat transfer between fluid and solid to predict the temperature-dependent viscosity. And they obtained some great results for floating ring bearings under high oil-supplied pressure. Kirk et al. [9, 10] experimentally investigated the vibration characteristics of the FRBs. San Andres et al. [11, 12] combined their previous work on the thermal effect modification of the lubricant fluid dynamic prediction with the rotor nonlinear dynamics and validated their prediction result using experiment data. They concluded the rotor potential large-amplitude subsynchronous vibration frequencies are 50% of the floating ring speed and 50% of the ring speed plus shaft speed.

Besides the thermal effect, two phase effect is also studied by researchers as an important factor in the FRBs. Tsuda et al. [13] initially observed air bubbles in the oil film in 1985. Air entrainment in the squeeze film damper is reported and validated by San Andres et al. [14, 15] in 2003, which remains as the standard until today. Song et al. [16-19] developed a gaseous cavitation model to predict the oil flow in FRB. Hatakenaka et al. [20] attempted to identify the causes of FRB problems and attributed them to cavitation [21]. They developed a method by using computational fluid dynamics (CFD) with the cubic-interpolated pseudoparticle (CIP) method to consider the air-oil two-phase flow.

Target of the research is the evaluation of flow transition in bearings by CFD. CFD method is increasingly used in the lubrication study [22-25] and cavitation model [26-30]. It is adopted in this work. This paper aims to reveal the mechanism of the phenomenon reported in Hatakenaka et al. [1]. CFD calculation is first conducted to validate the two phase model. Transit CFD calculation with mesh motion is conducted then to validate the CFD method and give prediction.

2. Calculation method

This work uses the CFD method to predict the lubrication flow. Cavitation is of vital importance in prediction of lubrication flow. Otherwise, a false low pressure zone will appear in the result. Two phase model is important for calculation of potential air entrainment in the FRB. In this part, the cavitation model and multiphase model used in this paper are introduced.

2.1. Cavitation model

The cavitation model is based on the solubility of air in lubricant [31,32]. It is assumed that air is fully dissolved in lubricant at the outside of the bearing, and at the divergent area of bearing clearance, the oil film pressure decreases, which leads to the change of solubility and the emission of air. The volume of air emission can be expressed as follows:

$$\tilde{V}_{air} = \left(\delta_{surround} - \delta_{local}\right) V_{oil} \tag{1}$$

where $\tilde{V}_{air}$ is the standard volume of air emission, $\delta_{surround}$ and δ_{local} are the Bunsen solubilities of air at environment and oil film temperature.

So the volume fraction of air in the bearing clearance can be written as:

$$f_{air} = \frac{V_{air}}{V_{air} + V_{oil}} = \frac{1}{1 + \frac{p_{local}}{p_0} \cdot \frac{T_0}{T_{local}} \cdot \frac{V_{oil}}{\tilde{V}_{air}}} = \frac{1}{1 + \frac{p_{local}}{p_0} \cdot \frac{T_0}{T_{local}} \cdot \frac{1}{\delta_{surround} - \delta_{local}}} \tag{2}$$

Then lubricant density and viscosity can be given by:

$$\rho = (1 - f_{air})\rho_{oil} + f_{air}\rho_{air} \tag{3}$$

$$\mu = (1 - f_{air})\mu_{oil} + f_{air}\mu_{air} \tag{4}$$

Bunsen solubility of air in oils are:

$$\delta = e^{-2.476+\frac{250.8}{T}} \frac{p}{p_0} \tag{5}$$

where p_0 is the atmosphere pressure. Substituting into Eqn.(2), then:

$$f_{air} = \frac{1}{1 + \frac{1}{\frac{T_{local}}{T_0}\left(e^{-2.476+\frac{250.8}{T_{surround}}} \cdot \frac{p_{surround}}{p_{local}} - e^{-2.476+\frac{250.8}{T_{local}}} \right)}} \tag{6}$$

The relationship between oil film pressure and f_{air} has been set up, and the lubricant properties can be calculated, by which the cavitation region can be calculated during the solving of N- S equations.

2.2. Multiphase model

For 3D CFD, three-dimensional Navier-Stokes equations are solved to obtain the pressure and temperature of two oil film. N-S equations are given as follows:

$$\frac{\partial \rho}{\partial t} + \nabla \cdot (\rho U) = 0 . \tag{7}$$

$$\frac{\partial (\rho U)}{\partial t} + \nabla \cdot (\rho U \otimes U) = -\nabla p + \nabla \cdot \tau + S_M . \tag{8}$$

where τ is shear stress tensor, given as follows:

$$\tau = \mu\left(\nabla U + (\nabla U)^T - \tfrac{2}{3}\delta \nabla \cdot U \right) . \tag{9}$$

S_M is source term of momentum equation. Energy equation is:

$$\frac{\partial \rho h_{tot}}{\partial t} - \frac{\partial \rho}{\partial t} + \nabla \cdot (\rho U h_{tot}) = \nabla \cdot (\lambda \nabla T) + \nabla \cdot (U \cdot \tau) + S_E \tag{10}$$

where h_{tot} is total enthalpy of fluid. λ is thermal conductivity of the fluid. S_E is energy flow in energy equation.

In order to simulate the air invasion flow into the oil film. 3D multiphase CFD has to be carried out. There are many models to predict the multiphase flow. In this research, homogeneous Eulerian-Eulerian multiphase model is taken for its strength in predicting the multiphase flow whose velocity fields are shared by each phase. This model are less computationally costly than other models.

Multiphase flow is calculated with the notion of volume fraction r_α. The volume that α phase takes in a small volume V is given by:

$$V_\alpha = r_\alpha V \tag{11}$$

For a given process of transportation, transported quantities are shared in homogeneous multiphase flow. So the bulk transport equations rather than the individual phasic transport equations are solved to get the flow field. Simply solving equation (1)(2) with special consideration of the density and viscosity given as following:

$$\rho = \sum_\alpha r_\alpha \rho_\alpha . \tag{12}$$

$$\mu = \sum_\alpha r_\alpha \mu_\alpha . \tag{13}$$

And volume conservation equations are:

$$\sum_{\alpha} r_{\alpha} = 1 \tag{14}$$

In order to close the equation system. Constraints on the pressure are given. It is assumed that all phases share the same pressure field:

$$p_{\alpha} = p \tag{15}$$

For calculation of heat transfer, different from the transport processes of mass and momentum, the shared field disagreed with transport property. It is the temperature that is shared but enthalpy that is transported. Hence, for multi-phase CFD, energy equation has to be solved individually by each phase. And in order to obtain one temperature field from different phase. A large interphase heat transfer term is then assumed

2.3. Dynamic mesh method

The Boundary motion is defined by the rigid body motion. Boundaries adjacent to the floating ring is moved with the motion of the floating ring motion. Boundary adjacent to the shaft is moved with the shaft. The motion of the rigid body is calculated by:

$$\frac{dP}{dt} = F \tag{16}$$

$$\frac{d\Pi}{dt} = T \tag{17}$$

where P represents the linear momentum. Π represents the angular momentum. F is the force acting on the rigid body. T is the torque acting on the rigid body. The force acting on the rigid body includes hydrodynamic and gravitational forces and moments on the rigid body. These forces are computed by numerical integration of pressure and shear stress over the rigid body's surfaces. Dynamic mesh method is adopted in the commercial software ANSYS CFX. The mesh deformation option in CFX enables the specification of the motion of nodes on boundary or subdomain regions of the mesh. The motion of all remaining nodes is determined by the mesh motion model, which is the displacement diffusion model. With this model, the displacements applied on domain boundaries or in subdomains are diffused to other mesh points by solving the equation:

$$\nabla\cdot\left(\Gamma_{disp}\nabla\delta\right) = 0 \tag{18}$$

where δ is the displacement relative to the previous mesh locations and Γ_{disp} is the mesh stiffness, which determines the degree to which regions of nodes move together. This equation is solved at the start of each outer iteration or time step for steady state or transient simulations, respectively.

3. Calculation setting

The calculation domain of FRB consists of two oil films and an oil supply pipe. The calculation domain is shown in the figure 2(a). The parameters are shown in the table 1. The bearing parameters used in the simulation is exactly the same as with those in the experiment by Hatakenaka et al. [1].

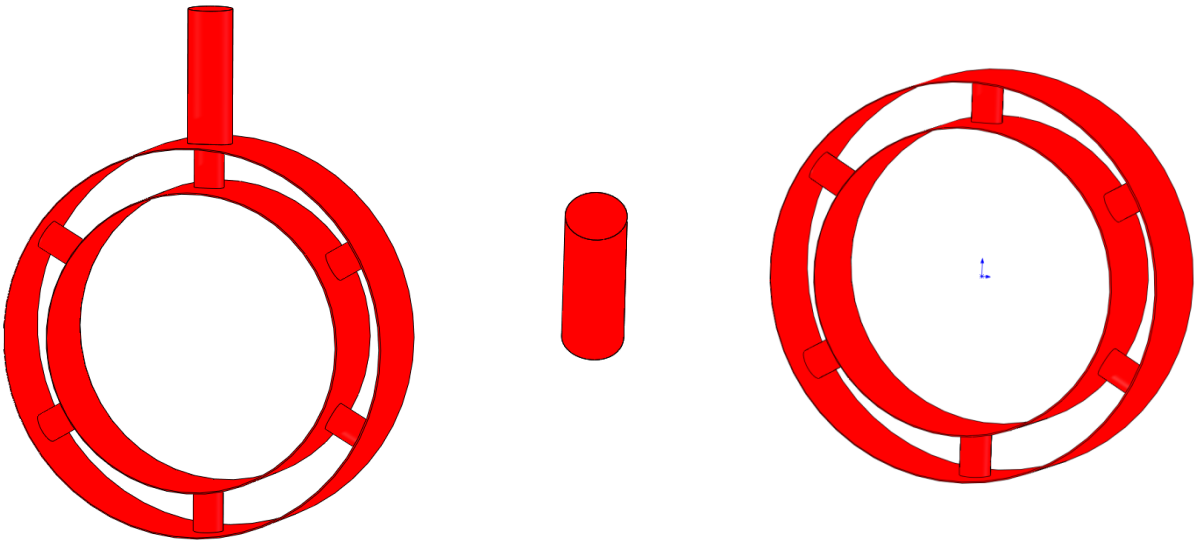

(a) Entire fluid domain (b) Oil supply pipe (c) Oil films

Figure 2. Fluid domain

Given the complicated shape of the fluid domain, the entire domain should be divided to keep the mesh in good quality. In this work, the domain is divided into two parts, namely, oil films and oil supply pipe, as shown in figure 2(b) and (c). These parts are discretized into a structured mesh as shown in figure 3. Cut view of the mesh is shown in the figure 4.

Table 1. FRB parameters

Diameter of shaft /mm	20
Outer diameter of ring /mm	26
Inner clearance /mm	0.08
Outer clearance /mm	0.08
Width of ring /mm	8.0
Number of Holes on the ring	6
Supplied pressure / kPa	3

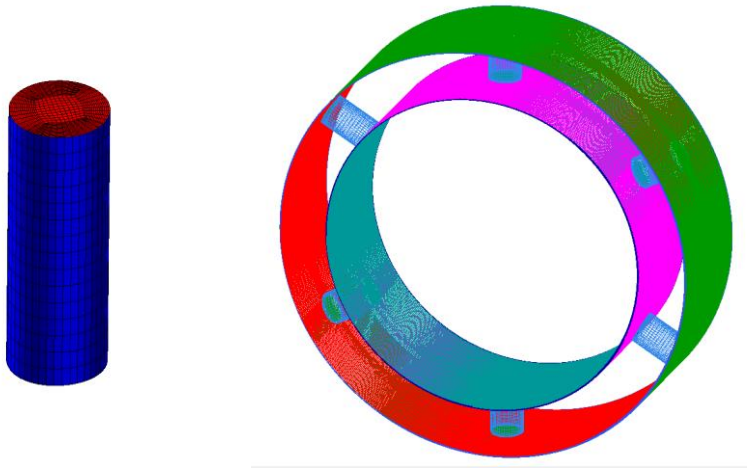

(a) Oil supply pipe (b) Oil films

Figure 3. Mesh used in the calculation

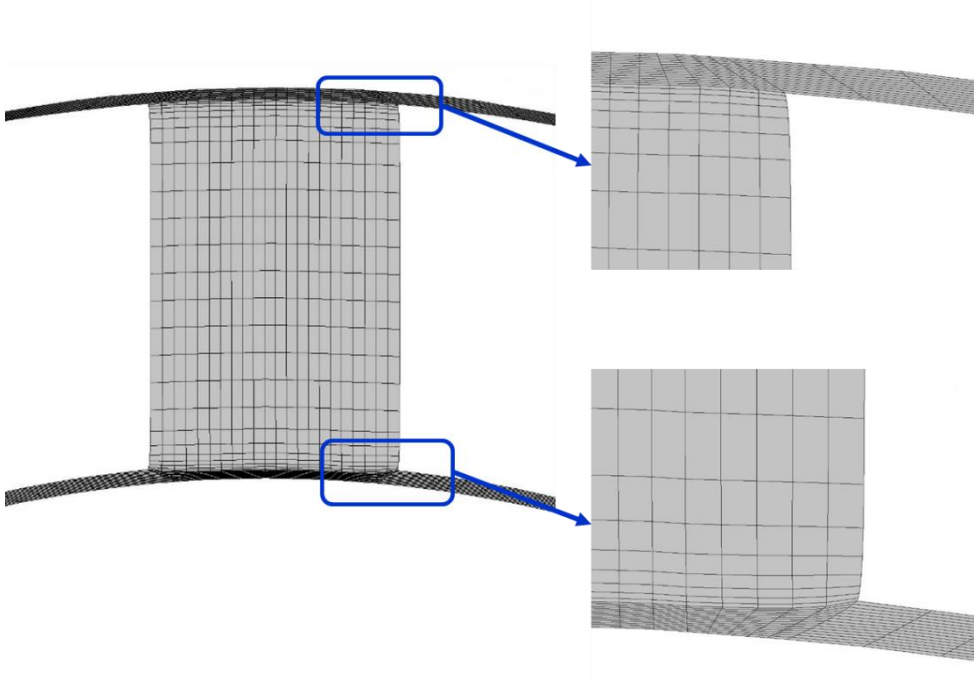

Figure 4. Detail of the mesh motion

This work employs the Grid Convergence Index (GCI) method for grid independence validation as recommended by ASME. This method provides a dependable method to estimate the uncertainty error of the grid. The ring-to-shaft speed ratio is regarded as an important parameter in FRB calculation. The torques on the inner and outer surfaces of the ring are the variables that determine the floating ring rotation speed; thus, they are selected as parameters to be verified. The element numbers of three sets of mesh are 0.50, 1.21, and 3.13 million. The three sets of grids are marked as 1, 2, and 3, and they are subscripted. Define the representative mesh size h as the cube root of the total volume divided by number of elements. Afterwards, define the mesh refinement factor r_{ij} as the ratio of representative mesh size of two meshes as follows:

$$r_{ij} = h_i / h_j . \tag{19}$$

The grid refinement factors r_{21} and r_{32} are larger than 1.3, as required by the GCI method. The analysis results are shown in table 2. The errors of the torque on the inner and outer surfaces of the ring are 0.105% and 1.921%, respectively. This finding indicates that this grid can precisely predict the torque on the ring. Thus, the number of elements is adopted as 1.21 million.

Table 2. GCI method analysis result

	Inner surface torque	**Outer surface torque**
Total volume	2.11E-7 m^3	
Refinement factor	r_{21} = 1.343	r_{32} = 1.373
Φ_1	−0.01431	0.007416
Φ_2	−0.01395	0.007651
Φ_3	−0.004703	0.007141
Error	0.105%	1.921%

Table 3. Mesh quality property

Domain name	Oil films	Oil supply pipe
Minimum skew angle (°)	16.4	54.1
Maximum aspect ratio	103	14.1

The quality of the 1.21 million mesh is shown in table 3. The maximum aspect ratio is about 100. This value is of good quality, particularly considering that the fluid domain itself has a large aspect ratio. The minimum skew angles in the oil film and oil supply pipe domains are 16.4 and 54.1, respectively. The skew angles are sufficiently large in both domains.

Many researches on CFD code [33-36] with all–speed Roe scheme [37-40] and discontinuous Galerkin reconstruction methods [41-44] is conducted to give precise prediction of the fluid flow. In this work, commercial software CFX is adopted for its high flexibility and fidelity. In the simulation, the boundary condition is set to be the same as that in the experiment conducted in study [1]. The oil feeding pressure and temperature are specified at the inlets of the feeding pipe at 3000 Pa and 40 ℃, respectively. Pressure at the circumferential outlet of the inner and outer oil films is provided as atmospheric pressure. The walls are all set to be adiabatic no-slip wall, unless specified. Considering the seal structure of the house, air entrainment is difficult to occur in the outer film outlet. Thus, it is assumed that air entrainment does not occurs in the outer film. The outer film outlet is set as 100% oil. Furthermore, the inner film outlet is open to the surrounding environment. The inner film outlet condition is assumed to be 100% air. Experiment [1] is conducted using VG22 as lubricant. The dynamic viscosity of oil is expressed as

$$\nu_{\mathrm{eff}\_T} = 16537 \times T^{-1.788}, \tag{20}$$

where T is the temperature in ℃. Equation (11) is for oil VG22 at 40–90 ℃.

4. Results and analysis

4.1. Ring-to-shaft speed ratio

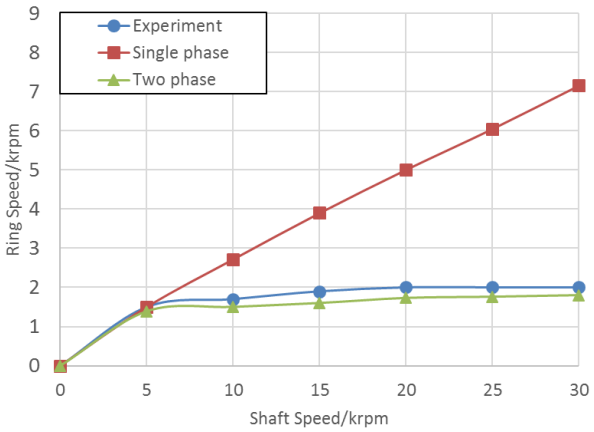

Figure 5. Ring speed change with shaft speed

Predicted results of the ring speed change with the shaft speed are shown in the figure 5. For the predicted results without two phase model, ring-to-shaft speed ratios remain constant. The predicted results are far from the experiment results. Results considering the two phase model are in consistence with the experiment results. These results show that the CFD method with two phase model is capable to predict the ring speed change with the shaft speed. CFD simulation with two phase model is capable

of capturing the air entrainment in the low oil-supplied pressure FRBs. Thus, results considering two phase flow matches with the experiment results.

4.2. Load condition

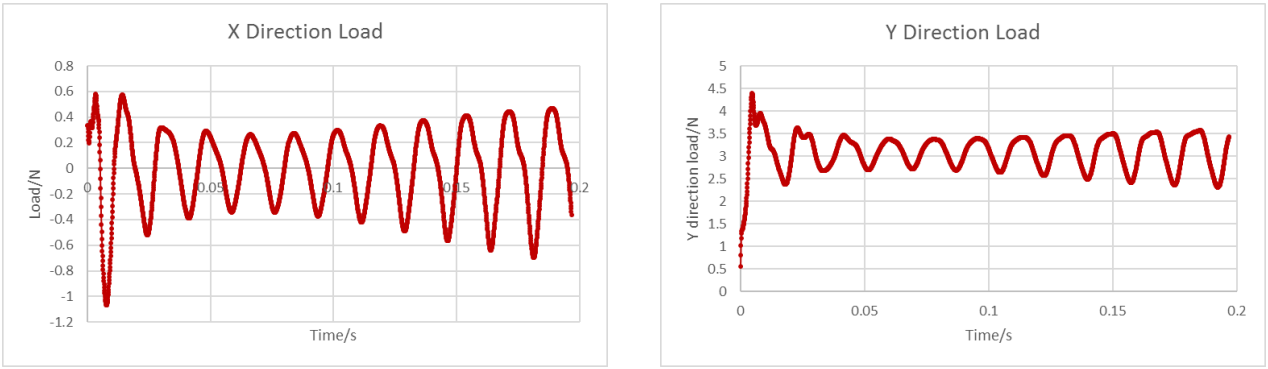

(a) Load on shaft

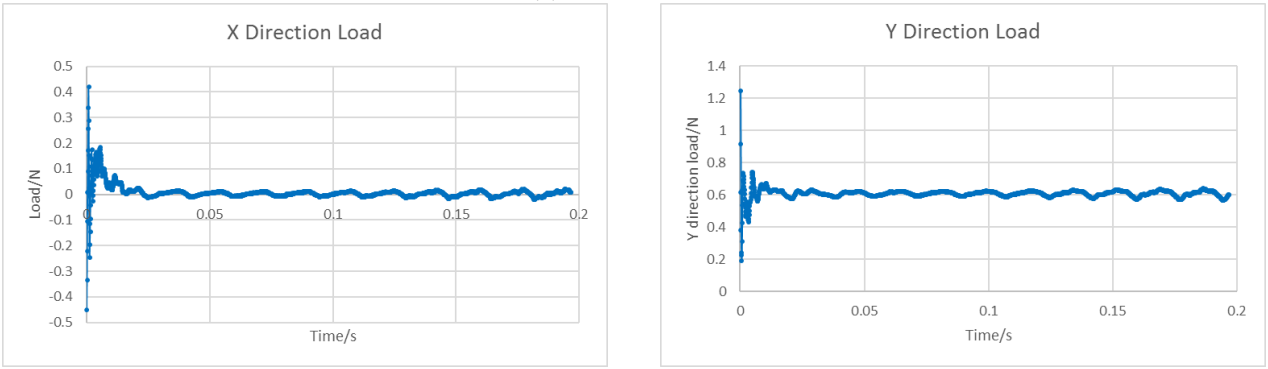

(b) Load on ring

Figure 6. Load change with time

Figure 6 shows the load on the shaft and the floating ring when shaft speed is 10 krpm. For the load on the shaft, the load in x direction vibrates around 0 and the load in y direction vibrates around the given load 3.1N. For the load on the ring, the load in x direction vibrates around 0 and the load in y direction vibrates around the given gravity force 0.6 N.

4.3. Bush and shaft position result

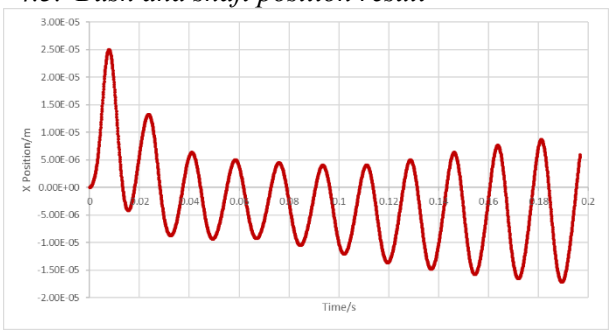

(a) X direction

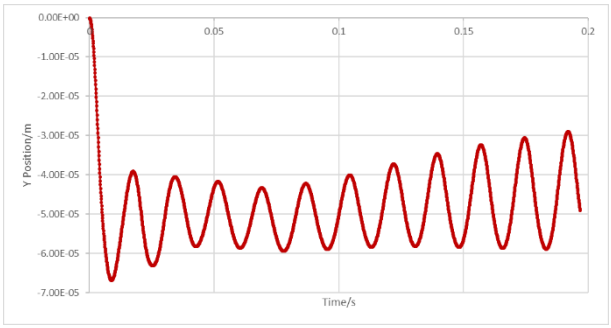

(b) Y direction

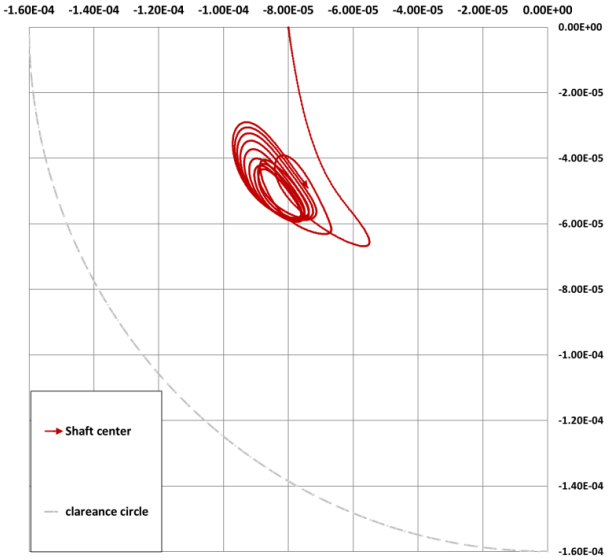

(c) Shaft limit cycle

Figure 7. Shaft position change with time

Figure 7 shows the shaft position when shaft speed is 10 krpm. Subsynchronous vibration can be captured in the current calculation model. And the shaft can reaches a limit cycle.

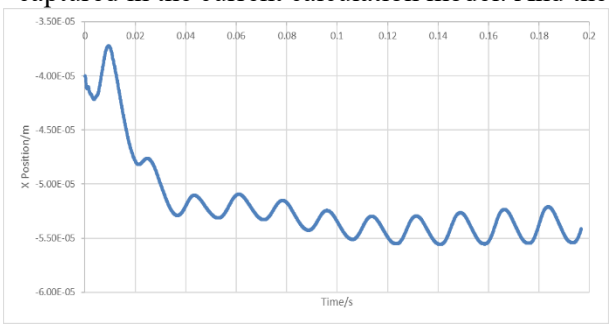

(a) X direction

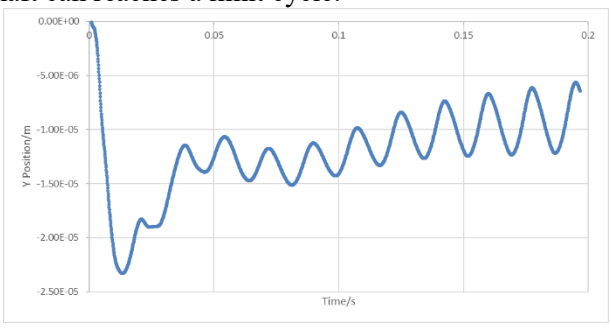

(b) Y direction

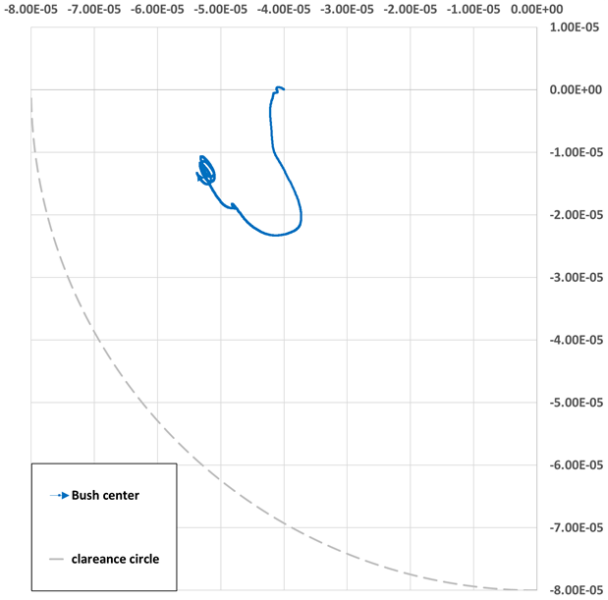

(c) Floating ring limit cycle

Figure 8. Ring position change with time

Figure 8 shows the ring position when shaft speed is 10 krpm. Ring vibrates at the same frequency as the shaft. Also, the ring can reaches a limit cycle. The limit cycle is relatively small compared with the shaft limit cycle.

4.4. Stability analysis

The dynamic characteristics are calculated when the shaft rotation speeds are 1 krpm and 10 krpm, include stiffness and damping coefficients. Stiffness coefficients are calculated by giving small perturbations of displacement either in the X or Y direction. The perturbations can lead to force on bearings, and in order to get damping coefficients, transient simulations are carried out. The results are shown in table 4 and 5. The k_{xy} and k_{yx} of 10 krpm is much larger than that of 1 krpm. These results also indicates that 10 krpm is much unstable than 1 krpm.

Table 4. Shaft stiffness and damping coefficients at 1 krpm

Stiffness coefficients	K_{xx} (N/m)	k_{xy} (N/m)	k_{yx} (N/m)	K_{yy} (N/m)
	6388.67	-88.71	68667.23	85628.79
Damping coefficients	C_{xx} (Ns/m)	c_{xy} (Ns/m)	c_{yx} (Ns/m)	C_{yy} (Ns/m)
	26.95	49.36	-1447.78	399.32

Table 5. Shaft stiffness and damping coefficients at 10 krpm

Stiffness coefficients	K_{xx} (N/m)	k_{xy} (N/m)	k_{yx} (N/m)	K_{yy} (N/m)
	-84079.71	-41717.30	-1045803.77	-1727330.86
Damping coefficients	C_{xx} (Ns/m)	c_{xy} (Ns/m)	c_{yx} (Ns/m)	C_{yy} (Ns/m)
	33.00	-49.28	1728.43	-1541.41

5. Conclusion

In this research, CFD prediction method of FRBs is constructed and validated. Major conclusions are as follows:

Two phase flow model is important in predicting the performance of the FRBs under low oil-supplied pressure condition. Method considering two phase flow can obtain precise ring-to-shaft speed ratio results.

CFD method with mesh motion can capture the motion of the floating ring and shaft. It is capable of simulating the shaft and ring vibration. The vibration result is in consistence with the experiment.

For the given FRB, stability analysis shows that shaft at 10 krpm is much unstable than that at1 krpm. This result also matches with the experiment. This CFD prediction method shows great capacity of reveal the vibration details of the FRB.

References

[1] Hatakenaka, K., and Yanai, H., 2008, "Stability in High-Speed Floating Bush Journal Bearings at Low Supplied Pressure (Part 1)-Effect of Oil Groove and Holes into Inner Oil Film and Slope at Bush Inner Side End on Stability", *Journal of Japanese Society of Tribologists*, **53**(8), pp. 536-543.

[2] San Andres, L., Rivadeneira, J. C., Gjika, K., Groves, C., and La Rue, G., 2007, "Rotordynamics for small turbochargers supported on floating ring bearings-Highlights in bearing analysis and experimental validation", *Journal of Tribology*, **129**(2), pp. 391-397.

[3] Kirk, R. G., Mondschein, B., Alsaeed, A. A., Gallimore, D., Framk, A., Crouch, J., Tiller, M., Vo, T., Thrush, K., and Lloyd, R., OCT 17-20, 2010, "Influence of Turbocharger Bearing Design on Observed Linear and Nonlinear Vibration", *ASME International Joint Tribology Conference*, San Francisco, CA, Proceedings of the STLE/ASME International Joint Tribology Conference, 2010.

[4] Tatara, A., 1970, "An Experimental Study of the Stabilizing Effect of Floating-Bush Journal Bearings", *Bull. JSME*, **13**(61), pp. 858-863.

[5] Trippett, R. J., 1986, ''Measured and Predicted Friction in Floating-Ring Bearings'', *SAE Trans*., **95**, pp. 1470–1476.

[6] Trippett, R. J., and Li, D. F., 1984, ''High-Speed Floating-Ring Bearing Test and Analysis'', *ASLE Trans*., **27**(1), pp. 73–81

[7] San Andres, L., and Kerth, J., 2004, "Thermal effect on the performance of floating ring bearings for turbochargers", *Journal of Engineering Tribology*, **218**(5), pp. 437-450.

[8] San Andres, L., Barbarie, V., Bhattacharya, A., Gjika, K., 2012, "On the Effect of Thermal Energy Transport to the Performance of (Semi) Floating Ring Bearing Systems for Automotive Turbochargers", *Journal of Engineering for Gas Turbines and Power*, **134**(10), pp. 1-10.

[9] Kirk. R. G., Komhauser, A. A., Sterling, J., and Alsaeed, A., 2010, "Turbocharger On-engine Experimental Vibration Testing", *Journal of Vibration and Control*, **16**(3), pp. 343-355.

[10] Kirk, R. G., Alsaeed. A., Liptrap, J., Lindsey, C., Sutherland, D., Dillon, B., Saunders, E., Chappell, M., Nawshin, S., Christian, E., Ellis, A., Mondschein, B., Oliver, J., Sterling, J., 2008, "Experimental Test Results for Vibration of a High Speed Diesel Engine Turbocharger", *Tribology Transactions*, **51**(4), pp. 422-427.

[11] San Andres, L., Rivadeneira, J. C., Gjika, K., Groves, C., La Rue, G., 2007, "A Virtual Tool for Prediction of Turbocharger Nonlinear Dynamic Response: Validation Against Test Data", *Journal of Engineering for Gas Turbines and Power*, **129**(4), pp. 1035-1046.

[12] Holt, C., San Andres, L., Sahay, S., Tang, P., La Rue, G., Gjika, K., 2005, "Test response and nonlinear analysis of a turbocharger supported on floating ring bearings", *Journal of Vibration and Acoustics*, **127**(2), pp. 107-115.

[13] Tsuda, K., and Takahashi, T., 1985, "Observation of Oil Film Disappearance Between Shaft and Fast Rotating Bush Lubricated From Outside", *Journal of Japan Society of Lubrication Engineers*, **30**(1), pp. 69-72.

[14] San Andres, L., Diaz, S. E., 2003, " Flow visualization and forces from a squeeze film damper operating with natural air entrainment", *Journal of Tribology*, **125**(2), pp. 325-333.

[15] Diaz, S., San Andres, L., 2001, " A model for squeeze film dampers operating with air entrainment and validation with experiments", *Journal of Tribology*, **123**(1), pp. 125-133.

[16] Song, Y., Gu, C. W., and Ren, X., 2015, "Development and validation of a gaseous cavitation model for hydrodynamic lubrication", *Journal of Engineering Tribology*, **229**(10), pp. 1227-1238.

[17] Song, Y., Li, X. S., and Gu, C., 2010, "Cavitation Model for Oil Film Bearings". *J. Tsinghua Univ.*, **50**(7), pp. 1047-1052

[18] Li, X. S., Song, Y., Hao, Z. R., and Gu, C. W., 2012, "Cavitation Mechanism of Oil-Film Bearings and Development of a New Gaseous Cavitation Model Based on Air Solubility", *Journal of Tribology*, **134**(3), pp. 031701.

[19] Wang Yan, Ren Xiao-Dong, Li Xue-Song and Gu Chun-Wei, 2017, "Numerical Investigation of Air–Oil–Thermal Coupling Mechanism in Floating Ring Bearings", *J. Tribol*, **140**(3), pp. 031701.

[20] Hatakenaka, K., Tanaka, M., and Suzuki. K., 2002, "A Theoretical Analysis of Floating Bush Journal Bearing with Axial Oil Film Rupture Being Considered", *Journal of Tribology*, **124**(3), pp. 494-505.
[21] Hatakenaka, K., Kasahara, K., and Ishibashi, N.,2008, "Bush Driving Torque in Inner Oil Film of Floating Bush Journal Bearing with Numerical Analysis for Multi-Phase Flow Being Applied". *Journal of Japanese Society of Tribologists*, **53**(9), pp. 612-620.
[22] Singhal, A. K., Athavale, M. M., Li, H. Y., Jiang, Y., 2002, " Mathematical basis and validation of the full cavitation model", *Journal of Fluids Engineering*, **124**(3), pp. 617-624.
[23] Gao, G. Y., Yin, Z. W., Jiang, D., Zhang, X. L., and Wang, Y. Z., 2016, "Analysis on design parameters of water-lubricated journal bearings under hydrodynamic lubrication", *Journal of Engineering Tribology*, **230**(8), pp. 1019-1029.
[24] Cheqamahi, J. M., Nili-Ahmadabadi, M., Akbarzadeh, S., Saghafian, M., 2016, "Numerical Analysis of Turbocharger's Bearing using Dynamic Mesh", *Journal of Applied Fluid Mechanics*, **9**(5), pp. 2545-2557.
[25] Gu, C., Wang, H., Ji, X., Li, X., 2016, "Development and application of a thermodynamic-cycle performance analysis method of a three-shaft gas turbine", *Energy*, **112**(1), pp. 307-321.
[26] Song, J., Gu, C., and Li, X., 2017, "Performance estimation of Tesla turbine applied in small scale Organic Rankine Cycle (ORC) system", *Applied Thermal Engineering*, **110**(5) , pp. 318-326.
[27] Tan, L., Zhu, B., Cao, S., Wang, Y., 2013, "Cavitation flow simulation for a centrifugal pump at a low flow rate", *Chinese Science Bulletin*, **58**(8), pp. 949-952.
[28] Tan, L., Zhu, B., Cao, S., Wang, Y., Wang, B., 2014, "Influence of prewhirl regulation by inlet guide vanes on cavitation performance of a centrifugal pump", *Energies*, **7**(2), pp. 1050-1065.
[29] Huang, D. G., Zhuang, Y. Q., 2008, "Temperature and cavitation", ImechE, *Journal of Mechanical Engineering Science*, **222**(2), pp. 207-211.
[30] Song, J., Li, X. S., Ren X. D., et al. 2018, "Performance analysis and parametric optimization of supercritical carbon dioxide (S-CO2) cycle with bottoming Organic Rankine Cycle (ORC)", *Energy*, **143** pp. 406-416.
[31] Song, Y., and Gu, C. W., 2015, "Development and Validation of a Three-Dimensional Computational Fluid Dynamics Analysis for Journal Bearings Considering Cavitation and Conjugate Heat Transfer", *Journal of Engineering for Gas Turbine and Power*, **137**(12), pp. 122502.
[32] Song, Y., Ren, X., Gu, C. W., and Li, X. S., 2015, "Experimental and Numerical Studies of Cavitation Effects in a Tapered Land Thrust Bearing", *Journal of Tribology*, **137**(1), pp. 011701.
[33] Huang, D., and Li, X., 2004, "Rotordynamic Characteristics of a Rotor with Labyrinth Gas Seals. Part 1: Comparison with Childs' Experiments", *Proceedings of the Institution of Mechanical Engineers – Part A: Journal of Power and Energy*, **218**(A3), pp. 171-177.
[34] Huang, D., and Li, X., 2004, "Rotordynamic Characteristics of a Rotor with Labyrinth Gas Seals. Part 2: a Non–Linear Model", *Proceedings of the Institution of Mechanical Engineers – Part A: Journal of Power and Energy*, **218**(A3), pp. 179-185.
[35] Wang H, Li X, Ren X, et al, 2017, "A thermodynamic-cycle performance analysis method and application on a three-shaft gas turbine", *Applied Thermal Engineering* , **127**, pp. 465–472.
[36] Li Y, Li X, and Ren X., 2016, "Aerodynamic optimization of a high expansion ratio Organic radial-inflow turbine", *Journal of Mechanical Science and Technology*, **30** (12), pp. 5485–5490.
[37] Li, X. S., and Gu, C., 2013, "Mechanism of Roe–Type Schemes for All–Speed Flows and Its Application", *Computers & Fluids*, **86**(5), pp. 56-70.
[38] Li, X. S., 2014, "Uniform Algorithm for All–Speed Shock–Capturing Schemes", *International Journal of Computational Fluid Dynamics*, **28**(6–10), pp. 329-338.

[39] Li X, and Gu X, 2010, "The momentum interpolation method based on the time-marching algorithm for All-Speed flows", Journal of Computational Physics , 229(20), pp. 7806-7818.
[40] Li, X. S., and Li, X. L., 2016, "All–Speed Roe Scheme For the Large Eddy Simulation of Homogeneous Decaying Turbulence", *International Journal of Computational Fluid Dynamics*, **30**(1), pp. 69-78.
[41] Ren, X., Xu, K., Shyy, W., and Gu,.C., 2015, "A Multi–Dimensional High–Order Discontinuous Galerkin Method Based on Gas Kinetic Theory for Viscous Flow Computations", *Journal of Computational Physics*, **292**(1), pp. 176-193.
[42] Ren, X., Gu, C., and Li, X., 2017, "Role of the Momentum Interpolation Mechanism of the Roe Scheme in Shock Instability", *International Journal for Numerical Methods in Fluids*, **84**(6), pp. 335-351.
[43] Liu, L. G., Gu, C. W., Ren, X. D., 2017, "An investigation of the conjugate heat transfer in an intercooled compressor vane based on a discontinuous Galerkin method", *Applied Thermal Engineering*, **114**(5), pp. 85-97.
[44] Li, X., Ren, X., and Gu, C., 2018, "Cures for expansion shock and shock instability of Roe scheme based on momentum interpolation mechanism", *Applied Mathematics and Mechanics (English Edition)*, DOI: 10.1007/s10483-017-2283-8.